



BUILDING ELECTRONIC BURSTERS WITH THE MORRIS–LECAR NEURON MODEL

ALEXANDRE WAGEMAKERS* and MIGUEL A. F. SANJUÁN

*Nonlinear Dynamics and Chaos Group,
Departamento Ciencias de la Naturaleza y Física Aplicada,
Universidad Rey Juan Carlos,
Tulipán s/n, 28933 Móstoles, Madrid, Spain
alexandre.wagemakers@urjc.es

JOSÉ M. CASADO

*Area de Física Teórica, Universidad de Sevilla,
Apartado de Correos 1065, 41080 Sevilla, Spain*

KAZUYUKI AIHARA

*Institute of Industrial Science, University of Tokyo,
153-8505, Tokyo, Japan
ERATO Aihara Complexity Modelling Project, JST,
151-0065, Tokyo, Japan*

Received December 20, 2005; Revised January 18, 2006

We propose a method for the design of electronic bursting neurons, based on a simple conductance neuron model. A burster is a particular class of neuron that displays fast spiking regimes alternating with resting periods. Our method is based on the use of an electronic circuit that implements the well-known Morris–Lecar neuron model. We use this circuit as a tool of analysis to explore some regions of the parameter space and to construct several bifurcation diagrams displaying the basic dynamical features of that system. These bifurcation diagrams provide the initial point for the design and implementation of electronic bursting neurons. By extending the phase space with the introduction of a slow driving current, our method allows to exploit the bistabilities which are present in the Morris–Lecar system to the building of different bursting models.

Keywords: Morris–Lecar; burster; neuron model.

1. Introduction

Nowadays the interface between electronic circuits and biological systems is attracting a great deal of research due to the enormous variety of potential applications of electronic devices to the general field of biomedical sciences. Even a connection of an electronic circuit with biological neurons is now possible [Lemasson *et al.*, 1999; Szûcs *et al.*, 2000]. As a consequence of this fact, new disciplines

such as biomedical engineering or bionics are reviving. From a theoretical viewpoint, the modeling of neurons is becoming more and more accurate, and the electrical behavior of neurons is well reproduced at a quantitative level by the increasingly complex mathematical models that are used in Computational Neuroscience. In this context, the modeling of neurons by means of electronic circuits is a steady growing field that presents rich

potentialities for the design of specific hardware that is able to display some useful characteristics for the processing of information in real time.

Experimentation on real neurons is a hard and expensive task, nevertheless part of these difficulties can now be solved to some extent with the help of artificial neurons. Computational neuroscientists can profit from the use of electronic devices as a tool for the exploration in real time of the behavior of neuron models [Horio & Aihara, 2002; Kohno & Aihara, 2005]. As a consequence, a network of artificial neurons can be emulated this way and tested in a real time environment. The devices connecting such circuits with biological neurons are called hybrid networks [Zeck & Fromherz, 2001; Simoni *et al.*, 2004], and the achievements of these tools in the biomedical sciences are immense. Artificial vision and audition [Vanschaik, 2001] or spinal cord stimulation for hemiplegic patient are some examples.

In this paper we propose an electronic implementation of a simple model of the giant barnacle muscle fiber developed by Morris and Lécarr [1981]. The Morris–Lécarr model is a characteristic example of a simple dynamical system presenting a rich and wide variety of dynamical behaviors (see for instance [Morris & Lécarr, 1981] and [Rinzel & Ermentrout, 1989]). It uses only two dynamical variables to describe the state of the neuron and thus allows us a straightforward observation of the phase plane. In fact, with the help of an oscilloscope it is possible to visualize the attractors in real time. Moreover, depending on the parameters of the model, it presents Hopf (subcritical and supercritical), saddle-node and tangent bifurcations which can be easily observed. By examining these bifurcations, when two parameters are varied, we can observe some interesting codimension-2 bifurcations taking place in the system. A similar experimental work with electronic circuits has been achieved by [Binczak *et al.*, 2003] with a modified Fitzhugh–Nagumo neuron model and in [Patel *et al.*, 2000] in which a bifurcation diagram varying only one parameter for the Morris–Lécarr neuron model is carried out. The phase plane of the Morris–Lécarr model has been extensively explored in [Tsumoto *et al.*, 2006] with bifurcation analysis and numerical simulations. This paper investigates the bifurcations in a five-dimensional space. Nevertheless the method proposed here is experimental.

We have analyzed the Morris–Lécarr phase plane to develop a method to obtain bursting

behavior. Bursters are a class of neurons which are present in many areas of the brain and whose autonomous activity displays periods of fast spiking alternated with resting or silent intervals. Furthermore, an external current can modulate the bursting response of those neurons and the coupling between bursters can lead to very complex synchronization patterns [Casado *et al.*, 2004].

The rather complex behavior of a burster is due to the coexistence of multiple attractors so that the phase point passes through a succession of different pseudo-attractors as it traces a closed orbit through the phase space [Chay *et al.*, 1995]. By finding out regions showing bistable behavior in the Morris–Lécarr model, we can construct a great variety of bursters [Izhikevich, 2000]. To do that, we take advantage of the hysteretic behavior of the system, leading to paths in the phase plane that are different depending on the way the parameter is varied. In our case the fundamental control parameter will be an external excitatory current delivered to the neuron. By choosing an appropriate dynamics for this current we can allow the system to hop between coexisting states thus giving rise to bursting activity patterns. In [Tsuji *et al.*, 2004] a design of a burster neuron based on the Fitzhugh–Nagumo model has been proposed, where an external forcing current is applied so that the model exhibits bursting activity. The parameters of the perturbation are based on the analysis of a two-parameter bifurcation diagram. In our work, since the excitation current is an internal variable of the system, the burster is autonomous. As examples of our methodology we present a square wave (or fold/homoclinic) burster, an elliptic (sub-Hopf/fold cycle) burster and a cycle/fold burster, all of them obtained from the dynamics of the Morris–Lécarr neuron model [Izhikevich, 2000].

The organization of the paper is as follow. In Sec. 2 we present the Morris–Lécarr model and its electronic implementation. The bifurcations of the circuit are analyzed in Sec. 3. In Sec. 4 we present a method for the design of electronic bursters and finally we summarize our results in Sec. 5.

2. The Morris–Lécarr Circuit

The Morris–Lécarr model was originally developed as a mathematical model of the giant barnacle muscle fiber [Morris & Lécarr, 1981]. It pertains to the class of the so-called conductance models and uses a calcium current, a potassium current and a leaky

ohmic current to phenomenologically describe the behavior of the muscle fiber. As the dynamics of the calcium channels is much faster than that of the potassium channels, we will consider the former always in the equilibrium state, thus reducing the model to the following system of two first order differential equations:

$$C \frac{dV_m}{dt} = -g_{Ca}^* M_\infty(V_m)(V_m - V_{Ca}) - g_K^* N(V_m - V_K) - g_L(V_m - V_L) + I \quad (1)$$

$$\frac{dN}{dt} = \lambda_N(V_m)(-N + G(V_m)), \quad (2)$$

where V_m is the membrane voltage, N is the activation variable of the slow potassium channels, and I is an external tonic current delivered to the neuron. Notice the voltage dependence on V_m of the time constant λ_N in Eq. (2), where its expression takes the following form:

$$\lambda_N(V_m) = \frac{1}{\phi} \cosh\left(\frac{V_m - V_3}{2V_4}\right). \quad (3)$$

On the other hand, g_{Ca}^* and g_K^* are the maximal conductances of the calcium and potassium channels, respectively, and g_L is a constant leak conductance. The conductances of the potassium and calcium channels vary in a sigmoidal way with the membrane voltage V_m . This dependence is introduced by the following functions $M_\infty(V)$ and $G(V)$:

$$M_\infty(V) = 0.5(1 + \tanh\left(\frac{V - V_1}{V_2}\right)), \quad (4)$$

$$G(V) = 0.5(1 + \tanh\left(\frac{V - V_3}{V_4}\right)), \quad (5)$$

where V_1, V_2, V_3 and V_4 will be considered as adjustable parameters.

As many other mathematical systems describing the electrical activity of the nerve membrane, a strategy based on the use of electronic circuits is well suited to implement its dynamical behavior. The above set of equations can be represented in a block diagram as shown in Fig. 1(a). This figure represents the equations of the model schematically and it will be the basis of the electronic circuit design that is presented in Fig. 1(b). In this figure we can see the three ionic currents which are generated by using the feedback of the voltage membrane V_m into the functional blocks. The calcium current has only one element, the sigmoidal shaped function

$G(V)$, whereas the potassium channel includes an integrator for the slow dynamics of this channel and also the variable time constant which depends on V_m . That means that the channel does not open and close instantaneously as the calcium channel does, but rather gradually, with a certain inertia. From the viewpoint of the electronics, this means a first order filter. These three currents are summed up and fed into an integrator to generate the membrane voltage.

In order to further reduce the complexity of the model we can make a strong approximation. Equation (2) representing the dynamics of the potassium channel includes a voltage-dependent time constant $\lambda_N(V_m)$. Implementing this parameter in the electronic circuit represents a difficulty. The hard point is to construct a voltage controlled resistor in order to modify the value of the time constant of a RC filter (or the first order filter). These components are mainly nonlinear and they introduce noise and undesirable harmonic components. Furthermore, this time constant has a complex influence in the equation. Nevertheless, when this function is set to a constant, the Morris–Lecar system of equations still exhibits interesting features like a Hopf bifurcation and spiking capabilities. Based on this observation we have reduced the original set of equations to a new set given by

$$C \frac{dV_m}{dt} = -g_{Ca}^* M_\infty(V_m)(V_m - V_{Ca}) - g_K^* N(V_m - V_K) - g_L(V_m - V_L) + I, \quad (6)$$

$$\frac{dN}{dt} = \tau^{-1}(-N + G(V_m)), \quad (7)$$

with the same functions $G(V_m)$ and $M_\infty(V_m)$ as in Eqs. (4) and (5). Here the parameter τ has a *constant* value, that is, it does not depend on voltage. This parameter has a critical role in the stability of the system because the Jacobian matrix of the linearized system around an equilibrium point has its eigenvalue depending on the parameter τ .

The proposed circuit is displayed in Fig. 1(b). It uses mainly linear components except for the analog multipliers and diodes. With this circuit we can now describe the experiments. The main logical blocks are delimited by dashed lines. The calcium block is made of a sigmoidal function, implemented with *pn* diodes, an operational amplifier, and an amplifier to adjust the gain and the bias. The output signal is fed into an analog multiplier (AD633) and multiplied with the tension V_m . The output of this

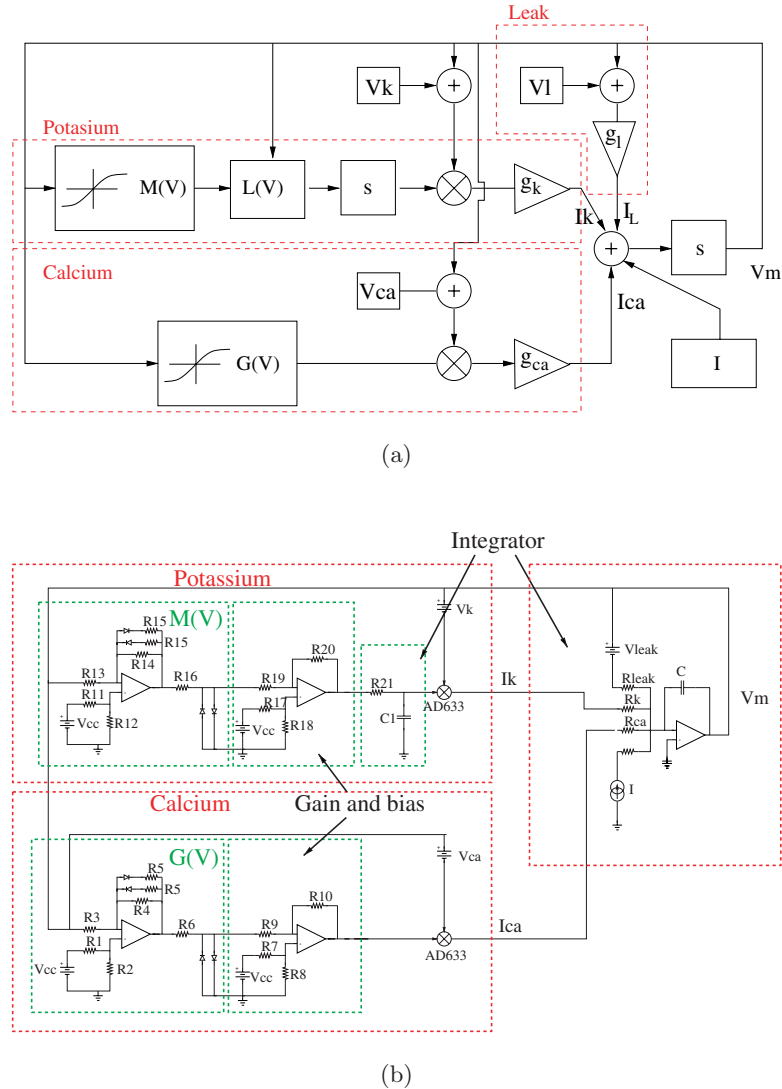


Fig. 1. (a) Block representation of the Morris–Lecar model. We represent the differential equations in a schematic way; blocks symbolize integrator, gains, transfer functions and multipliers. This logical representation is the basis of the implementation of the circuit. The blocks representing the ionic currents are delimited by dashed-lines; Eqs. (8) and (9) correspond to the currents I_{Ca} and I_K . All the currents are summed and fed into an integrator; the sum of the currents is comparable to Eq. (11). (b) Electronic scheme of the circuit simulating the Morris–Lecar model. The ionic currents are delimited by red dashed lines and correspond to the equivalent blocks in Fig. 1(a). The ionic currents I_{Ca} , I_K and I_L are summed and fed into an integrator so that the output is the membrane voltage V_m of the neuron model. The functions $G(V)$ and $M_\infty(V)$ are implemented with 1n4148 diodes and with UA741 OP-Amps.

block is the current I_{Ca} which expression is

$$I_{Ca} = M_\infty(V_m) \times (V_m - V_{Ca}). \quad (8)$$

The potassium current is quite similar, but now we use an analog integrator (a simple RC circuit). The expression of the ionic current can be described by the following two equations:

$$I_K = N(V_m - V_K), \quad (9)$$

$$\frac{dN}{dt} = \tau^{-1}(-N + G(V_m)). \quad (10)$$

The last block, the integrator, sums all the ionic currents and integrate them into a capacitor. The output of this circuit is the membrane voltage V_m . Thus, this variable is the solution of the following differential equation,

$$\frac{dV_m}{dt} = -I_K - I_{Ca} - I_L + I, \quad (11)$$

where I_L is a simple ohmic leak. In the following section we will explore the properties of this circuit.

3. Experimental Bifurcation Diagrams

In this section the equations used for the implementation of the circuit are slightly different. We have scaled the voltage in Eqs. (6) and (7) so that the observation of the voltage variable is made much easier. The scaling factor is a nondimensional number $\alpha = 0.120$. We can give the values of the fixed parameters that will be used next, unlike other parameters will be specified in each case: $V_{Ca} = 1\text{ V}$, $V_K = -0.66\text{ V}$, $V_L = 0.5\text{ V}$, $C = 20\text{ }\mu\text{F}$ and $C_1 = 1\text{ }\mu\text{F}$.

The experimental setup for the measurements of the bifurcation diagram is a simple AD/DA converter board. For a fixed set of parameters we construct the bifurcation diagram as a function of a varying external current. We slowly increase the current and observe the changes of the membrane voltage V_m .

In Fig. 2(a) we plot the maxima and minima of the membrane voltage to visualize the oscillatory behavior and stable states of the system. In this figure there appears a saddle-node bifurcation (point SN), a subcritical Hopf bifurcation (point HP) and a limit cycle (the spiking regime of the neuron), for clarity we schematically draw the corresponding three-dimensional phase space (N, V_m, I) in Fig. 2(b). By collecting a great

amount of these diagrams varying only one parameter and joining these one-dimensional diagrams in a two-parameter plot we can visualize how the bifurcations in the system evolve when a parameter is varied. Due to the complexity of the whole high-dimensional bifurcation diagram, we have used two-dimensional diagrams with one axis being I and the other one being another parameter of the model.

We have chosen three types of bifurcation diagrams which exhibit interesting features, (a) $I - V_3$ plane, where V_3 is the activation threshold of the potassium channel, (b) $I - V_4$ plane, where V_4 is the slope of the activation function for the potassium channel and, (c) $I - \tau$ plane, where τ is the time constant of the potassium channel. These parameters have a big influence on the model behavior as we describe below in each case.

3.1. $I - V_3$ diagram

In Fig. 3(a) we have plotted the corresponding bifurcations observed in the circuit when the parameters I and V_3 are varied. The different attractors and behaviors of the model are specified on the graphics with oscillations and stable nodes. The bifurcation diagram shows interesting global bifurcations, such as a Bogdanov–Takens bifurcation

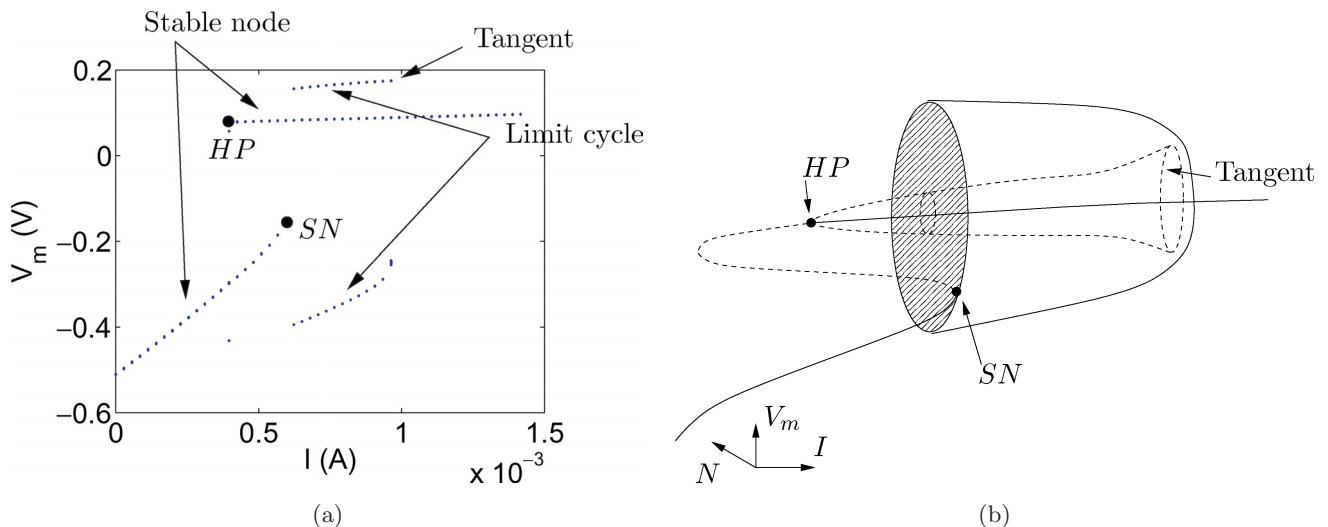


Fig. 2. (a) Experimental bifurcation diagram example in one dimension obtained by plotting the maxima and minima of the membrane voltage V_m as a function of the excitation current I . There we can observe three different attractors: two branches of stable fixed points, one of them starting from the left and another from the right of the panel, and a stable limit cycle (spiking behavior) coexisting with them between 0.5 and 1 mA. (b) This schematic diagram is the three-dimensional phase space (N, V_m, I) which corresponds to the experimental bifurcation diagram in (a). We can observe a saddle-node bifurcation (SN), a subcritical Hopf bifurcation (HP) and a tangent bifurcation of a limit cycle. The stable branches appear in solid lines while dashed lines represent unstable branches or unstable limit cycle.

(BT point on the panel) and a cusp bifurcation close to it. In fact, these two bifurcations are so close that at the selected scale they cannot be clearly differentiated. The first one represents the transition from a saddle-node bifurcation to a subcritical Hopf bifurcation, where this last bifurcation always lies near a cusp bifurcation. The cusp bifurcation appears when three equilibrium points, a saddle point and two nodes, collapse. In Fig. 3(b) we have plotted the bifurcation diagram obtained with the software XPP-AUTO; we have simulated Eqs. (6) and (7) with the parameters obtained from the circuit. Both diagrams are very similar albeit some little differences in the location of the bifurcations, for example, the experimental diagram is shifted left from 0.5 mA in comparison with the numerical diagram. There are several other differences due to the imprecisions and the noise in the circuit. The fine bifurcation structure detailed in Fig. 3(b) is too narrow to be observed in the circuit. The general aspect and the bifurcations are conserved which manifest that the circuit is robust.

In spiking neurons we have basically two types of excitability. The excitability represents the way the neurons begin to spike when an external current is gradually increased. In the first type of

neurons, the class I neurons, the neuron begins to spike with an almost zero frequency when the current is increased. In the class II neurons, the spiking begins at nonzero frequency. The change in the excitability of the neuron can be explained considering these bifurcations. As is well known, the Morris–Lecar model is able to support both class I and class II excitabilities. The change from the class I to class II excitability comes from a Bogdanov–Takens bifurcation which set the transition from a saddle-node bifurcation (class I excitability) to a subcritical Hopf bifurcation (class II). In our circuit we can control this parameter easily and so we can switch the type of excitability by only changing the parameter V_3 .

3.2. $I - V_4$ diagram

This bifurcation diagram which is shown in Fig. 4 is quite similar to the previous one in its structure. We observe the same characteristics and the same Bogdanov–Takens and cusp bifurcations (the BT bifurcation always lies near a cusp bifurcation). Moreover, a new type of codimension-2 bifurcation appears. This is a generalized Hopf bifurcation (also called a Bautin bifurcation) that corresponds to a

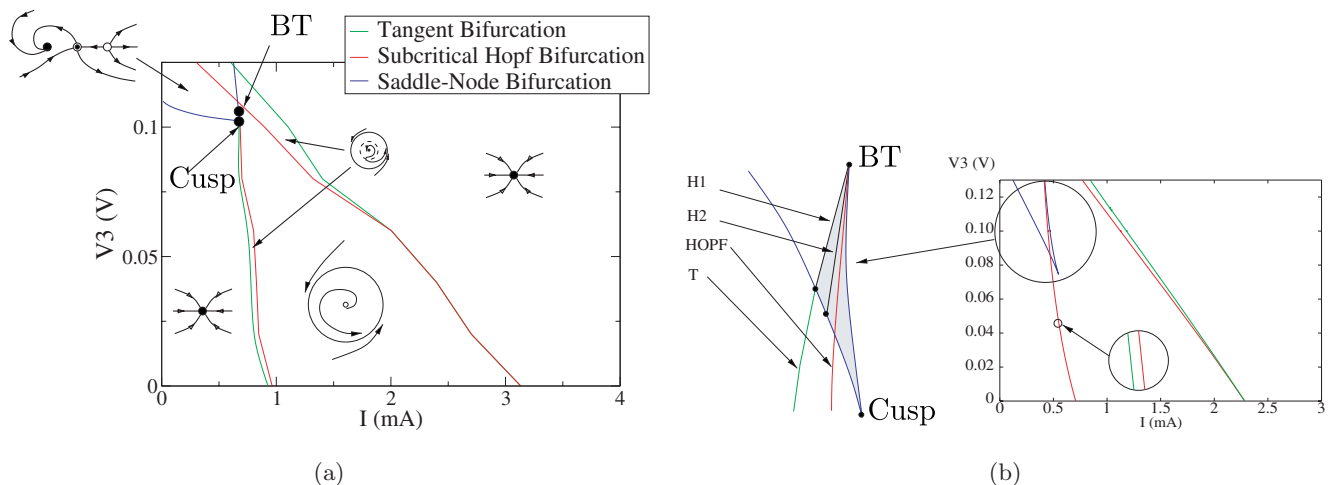


Fig. 3. (a) Experimental bifurcations in the $I - V_3$ plane. We observe a Bogdanov–Takens bifurcation (BT point) and a cusp bifurcation close to it. (b) The numerical results obtained from Eqs. (6) and (7) with the XPP-AUTO software. The color used for the bifurcations are the same as in Fig. 3(a). Both diagrams look very similar despite some differences in the place of the bifurcations due to the natural errors and distortions introduced by the circuit. The general aspect is conserved and also does the type of bifurcations, which manifests that the circuit is robust. We schematize the region of the circle which presents a complex bifurcation structure. The system in this region displays two homoclinic bifurcations. The first one is the homoclinic bifurcation of a stable limit cycle along the line H1 and the second is the bifurcation of an unstable limit-cycle along the line H2. In the shaded region we have a stable limit cycle. The Hopf bifurcation starts with a Bogdanov–Takens bifurcation on the saddle-node branch. In the inset of the figure we enlarge a part of the subcritical Hopf bifurcation so that the tangent bifurcation appears. At the selected scale the tangent bifurcation is hard to notice. The numerical simulation and the analog simulation correspond to the following parameters: $\tau = 2$ ms, $V_4 = 0.2$ V, $V_2 = 0.15$ V, $V_1 = 0$ V, $g_K^* = 8$ mS, $g_{Ca}^* = 4$ mS and $g_L = 2$ mS.

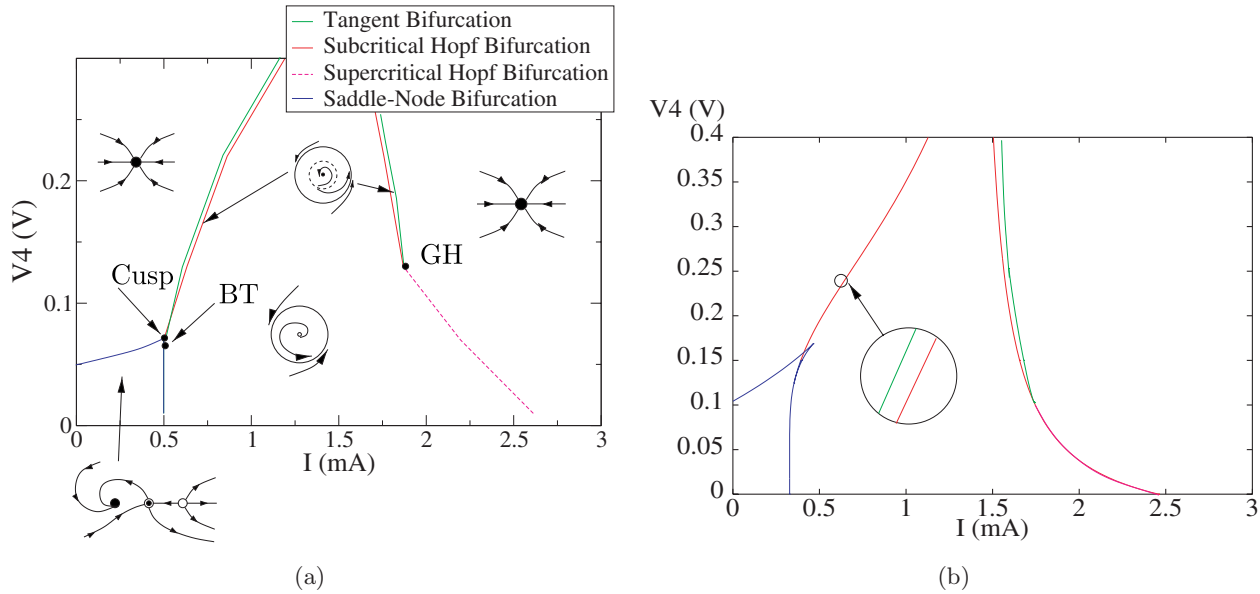


Fig. 4. (a) Experimental bifurcations in the $I - V_4$ plane. A Bogdanov–Takens lies in the plain and a cusp bifurcation is close to it. We found also a generalized Hopf bifurcation which represents the transition from a subcritical to a supercritical Hopf bifurcation. (b) This diagram represents the numerical simulation of Eqs. (6) and (7) for the same set of parameters. It is clear that the experimental diagram and the simulated diagram are very similar. Some mismatches between the two diagrams are due to the nonlinearities and to the experimental noise. The parameters are as follows: $\tau = 2$ ms, $V_3 = 0.06$ V, $V_2 = 0.15$ V, $V_1 = 0$ V, $g_K^* = 8$ mS, $g_{Ca}^* = 4$ mS and $g_L = 2$ mS.

transition from a subcritical to a supercritical Hopf bifurcation [Kuznetsov, 1998]. Once again the BT bifurcation changes the excitability of the neuron. We have two parameters that permit the control of the excitability of the model: V_3 and V_4 . As in Fig. 3 we also present the numerical result for the same set of parameters in Fig. 4(b). The numerical simulation obtained with XPP-AUTO agrees with the experimental diagram in Fig. 4(a). Moreover, the bifurcations are the same and their positions in the phase plane are similar in both diagrams. Some discrepancies appear between the two diagrams due to the approximations and the nonlinearities in the circuit as well as experimental noise. Nonetheless the diagram obtained with the circuit is satisfactory and illustrates well the model.

3.3. $I - \tau$ diagram

As it was mentioned before, the parameter τ is very important for the stability of the system because the dynamics of the potassium current is crucial to the stability of the model. It represents the time of repolarization of the membrane, or in other words, the time necessary for the membrane to return to the resting state after firing of a spike. In fact, by varying this parameter we can change dramatically the dynamics of the system. The position in the phase

space of the equilibrium points does not depend on τ , but the stability of each point is affected by this parameter. Figures 5(a) and 6(a) show experimental bifurcation diagrams where we observe bistable regimes. In Fig. 5(a), we have a big zone of bistability. On one side we have the bistability with a stable node and a limit cycle, and on the other side one with two stable nodes (along the line l_1). This particularity can be used for the design of a burster neuron as we will see next. Figure 5(b) shows the numerical simulation of Eqs. (6) and (7). This simulation validates the diagram obtained with the circuit, and the results are very close.

By modifying the parameter V_4 we obtain the new bifurcation diagram shown in Fig. 6(a). This diagram displays similar characteristics as the previous one. The saddle-node bifurcation on the limit cycle is independent of the parameter τ . In this figure we have an interesting bistable zone along the line l_2 where a limit cycle and a stable node coexist. The transition from one to another occurs through a subcritical Hopf bifurcation and a fold bifurcation. By using this particularity an elliptic burster can be constructed as it will be described in the next section. Along the line l_3 we have a bifurcation pattern identical to the one shown in Fig. 5(a) along the line l_1 . On one side we have a bistability between a limit

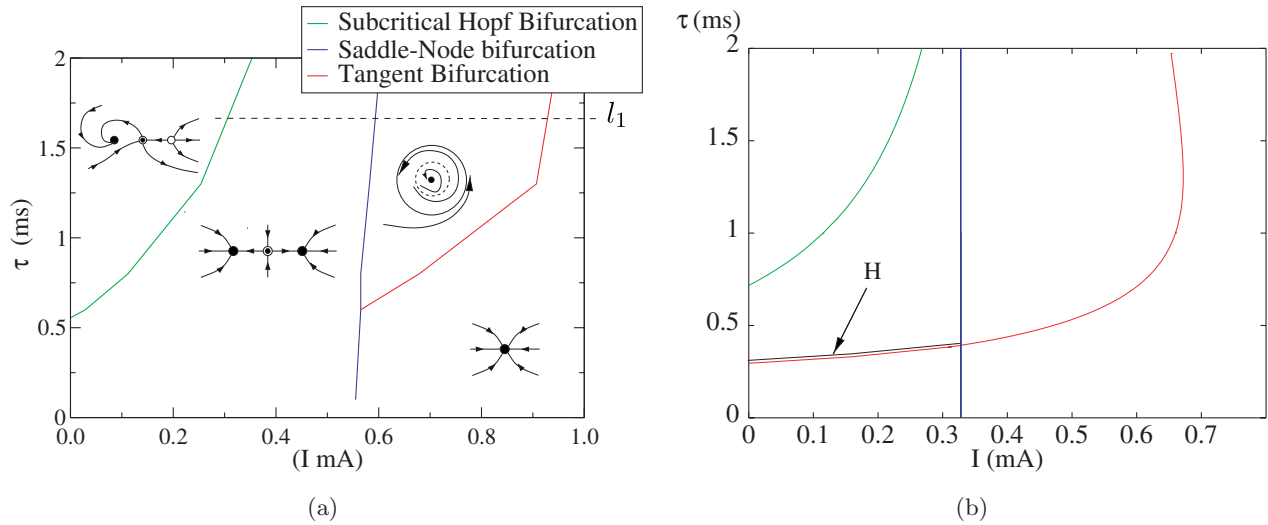


Fig. 5. (a) Experimental bifurcations in the $I - \tau$ plane. We have a large bistable zone represented by the coexistence of a stable node and a limit cycle (spiking behavior) due to a subcritical Hopf bifurcation. (b) This figure is the numerical result of Eqs. (6) and (7) with the same parameter set. The figures are almost identical but there is a systematic difference in the place of the bifurcations. The saddle-node bifurcation obtained with the circuit is shifted from 0.3 mA to the right. The black line marked as **H** on the diagram is the homoclinic bifurcation of a stable limit cycle, which bifurcation is difficult to observe in the circuit. This limit cycle region is too narrow. The parameters are as follows: $V_4 = 0.06$ V, $V_3 = 0.12$ V, $V_2 = 0.15$ V, $V_1 = 0$ V, $g_K^* = 8$ mS, $g_{Ca}^* = 4$ mS and $g_L = 2$ mS.

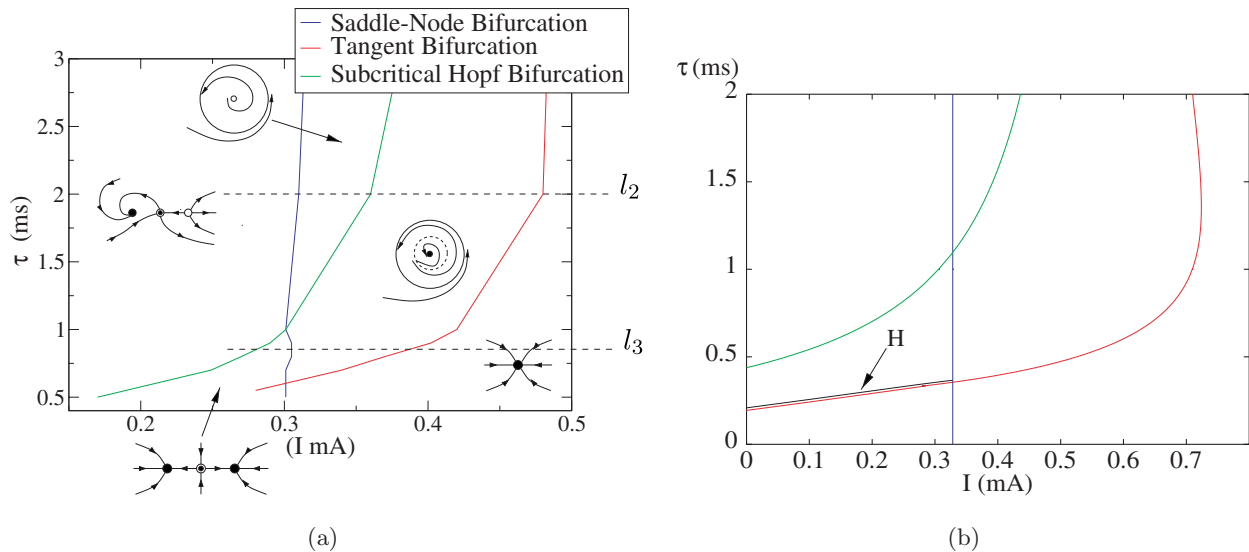


Fig. 6. (a) Experimental bifurcations in the $I - \tau$ plane. This diagram is very close to Fig. 5(a). In this figure we have changed slightly the parameters V_4 of the model and plot a new bifurcation diagram. We have the bistable zone with a stable node and a limit cycle, and a new zone appears where a single limit cycle (spiking behavior) is present. (b) The diagram plotted is the numerical result of the model equations with the same parameters used in the circuit. The two diagrams are very similar, while some differences appear in the diagram owing to the noise and the nonlinearities present in the circuit. The black line marked as **H** on the diagram is the homoclinic bifurcation of a stable limit cycle. This limit cycle region is too narrow to be observed with the circuit. The numerical values of the parameters are as follows: $V_4 = 0.1$ V, $V_3 = 0.12$ V, $V_2 = 0.15$ V, $V_1 = 0$, $g_K^* = 8$ mS, $g_{Ca}^* = 4$ mS and $g_L = 2$ mS.

cycle and a stable node and on the other between two stable nodes, although the transition from one to another in this case occurs through a saddle-node bifurcation. We have verified also this diagram with

the numerical simulation presented in Fig. 6(b) and both graphics correspond well.

The bifurcation diagram appearing in Fig. 7(a) presents a small bistable zone (the small triangle)

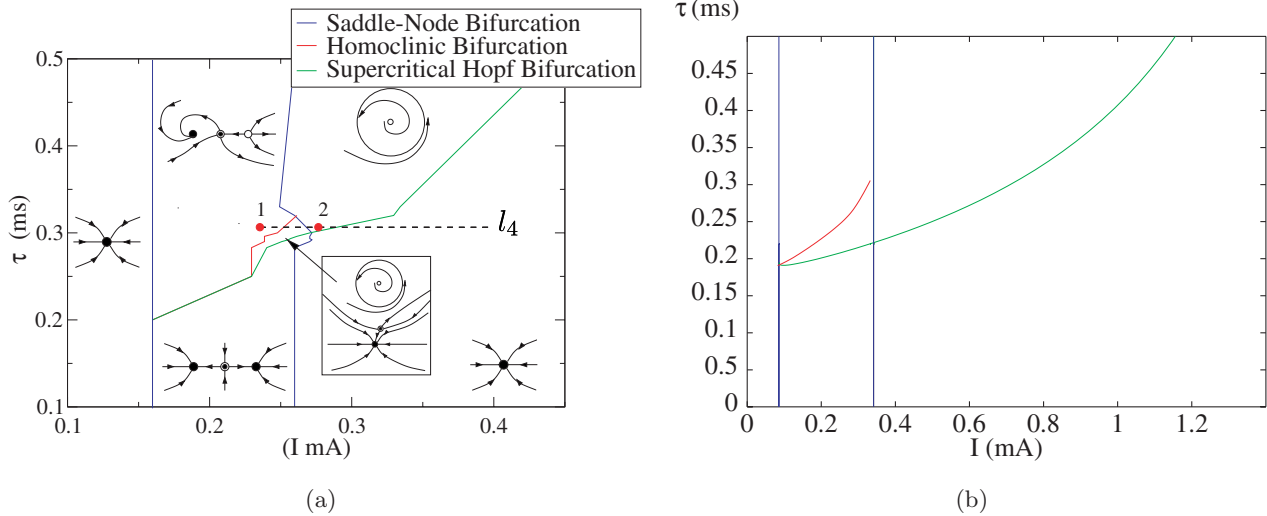


Fig. 7. (a) In this diagram we have a bistable zone with a limit cycle and a stable point. The transition from the limit cycle to the resting state occurs through a homoclinic connection to an unstable point. We can observe in the insets the different phase portrait and the attractors of the regions of the bifurcation diagram. The zone of bistability remains very small and is difficult to find out experimentally. (b) The figure shows the numerical result of Eqs. (6) and (7) with the same parameter set. The region of bistability in the triangle appears to be larger than in the experimental diagram, but in numerical simulations the noise is not present. So the region appears greater. The numerical values of the parameters are as follows: $V_4 = 0.07$ V, $V_3 = 0.032$ V, $V_2 = 0.15$ V, $V_1 = -0.028$ V, $g_K^* = 8$ mS, $g_{Ca}^* = 2.6$ mS and $g_L = 2$ mS.

where a stable node and a limit cycle coexist. If the system is on the stable branch, for example, at the point 1 on the diagram, when we increase the external current the attractor changes to a spiking regime after a saddle-node bifurcation (see point 2). On the other hand, when the current decreases the stable limit cycle collapses with a saddle point. The system describes a hysteresis loop as the trajectory is different as we increase or decrease the external current. Although this region of bistability always remains in a narrow range of parameters it can be a good candidate for the design of the square wave burster. The numerical simulation displayed in Fig. 7(b) with XPP-AUTO matches the result obtained experimentally. The homoclinic bifurcation seems longer than in the experimental diagrams and this region remains small but it is sufficient for our purpose.

4. The Design of Bursters

The previous experiments are the basis for the implementation of some models of bursting behavior. Since a burster works by switching between two (pseudo-)stable attractors (a limit cycle and a stable node, for example), we have to spot the bistable zones of the parameter space. Here the previous experimental work is essential, since we can visually find out the bistable regimes of the neuron model.

So, the first step is the search for bistable states where we can switch easily from one attractor to another by simply varying the external current. In the previous diagrams we had to look for a bistable regime along a horizontal line. For example, following the line l_2 in Fig. 6(a) we have a bistable behavior between a stable node and a stable limit cycle. When the external current is moved a hysteresis loop appears between the resting and the spiking states (Fig. 8).

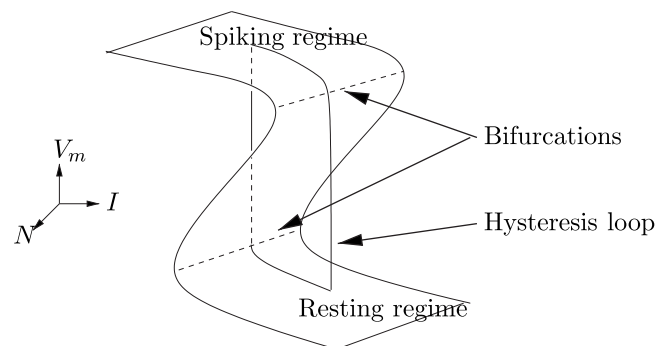


Fig. 8. Hysteresis loop of the burster. Observe that the system switches from a resting state to a spiking regime and back when the current I is changed. When the system is in the spiking regime, the current changes so that the state approaches the edge. As the system crosses the bifurcation on the edge the system returns to a resting state. The current in this state changes its direction and the state approaches the lower edge. The burster oscillates between these two states.

This hysteresis loop leads to transitions from the resting state to the spiking regime and back. Once we have chosen two coexisting states as good candidates for the switching, we introduce a new differential equation in our system to allow this switching to take place autonomously. This new equation governs the slow current I , and is given as follows:

$$\frac{dI}{dt} = \frac{1}{R_a R_b C_2} (V_m - V_{th}), \quad RC \gg \tau. \quad (12)$$

The introduction of the new variable $I(t)$ allows us to switch the whole dynamics from one attracting state to another one by a suitable election of values of R_b and V_{th} . Observe that now I is really an “internal” variable of the extended dynamical system. Equation (12) is implemented by using a simple operational amplifier in integrator mode. In

order to develop our method, we start by marking the interesting bistable zone on the bifurcation diagram (horizontal line l_1 on Fig. 5(a)) and extracting the corresponding projection in one dimension (current versus amplitude in Fig. 2). Setting the voltage threshold V_{th} in Eq. (12) is a rather difficult task because the integrated current must decrease when the burster is spiking and must increase when the burster is in its resting state. The parameter is tuned manually so that we obtain the desired behavior. The resulting waveform of this current for the square-wave burster is shown in Fig. 9. Notice that the current I is increasing when $\langle V_m \rangle$ (where $\langle \cdot \rangle$ holds for the mean value) is above the threshold and decreasing when it is below V_{th} . The second parameter R_b is important for the time constant of the equation; it determines the speed of the slow

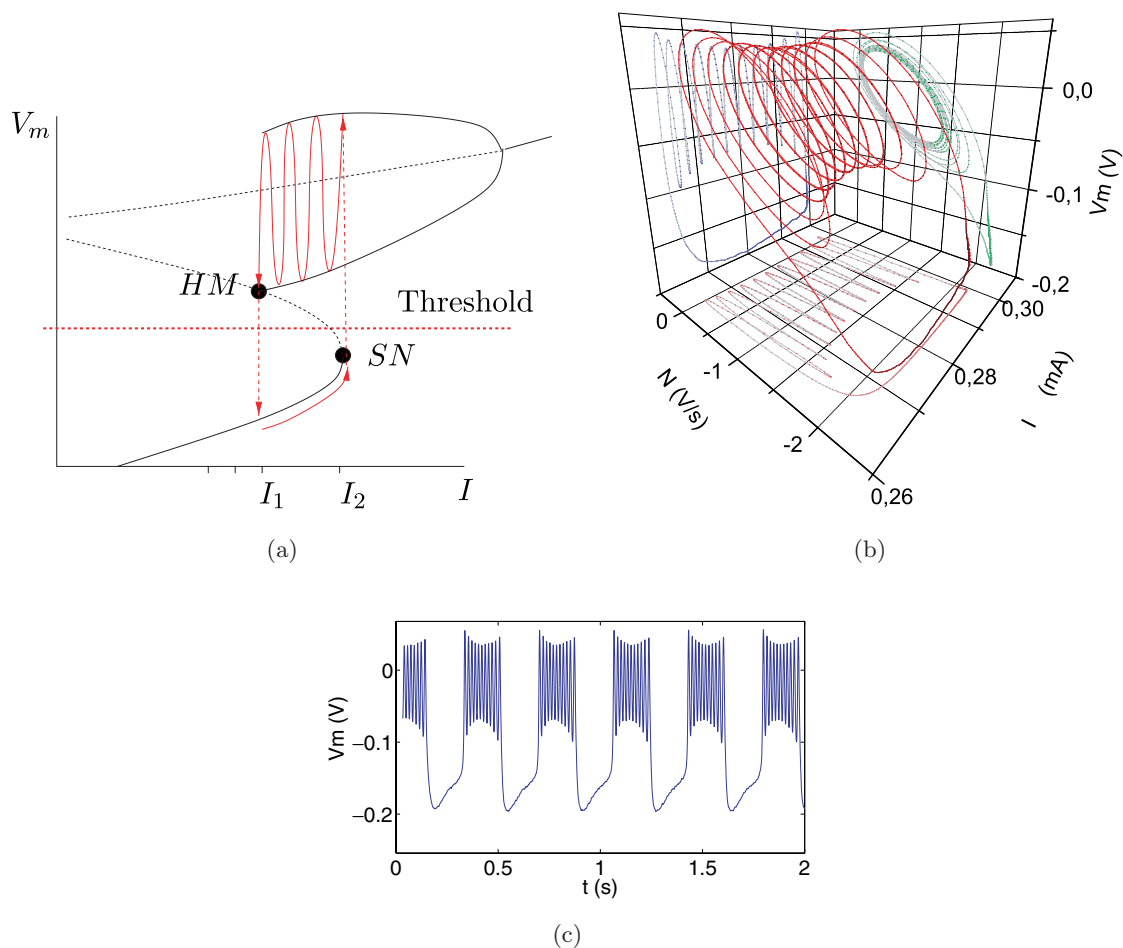


Fig. 9. (a) Dynamical behavior of the square-wave burster. The figure represents the bifurcation diagram of the Morris–Lecar model as a function of I . The bursting regime appears through a fold bifurcation for the passage from the stable node to the limit cycle and through a homoclinic connection when the cycle loses its stability and gets back to the resting state; (b) 3D view of the orbit in the space (I, N, V_m) . The parameter values are as follows: $\tau = 0.03$ s, $V_4 = 0.07$ V, $V_3 = 0.028$ V, $V_2 = 0.15$ V, $V_1 = -0.032$ V, $g_K^* = 8$ mS, $g_{Ca}^* = 1.38$ mS, $g_L = 2$ mS, $C_2 = 1 \mu F$, $R_a = 4.3$ k Ω and $R_b = 13.7$ k Ω . (c) Time series of the membrane voltage corresponding to the output of the circuit.

driving current. If this parameter is set too high, the oscillations are weak. If the constant is too low the system can switch to another attractor.

We present in the next sections three different kind of bursters whose differences are due to the bifurcations involved. Biological equivalence exist for two of the three bursters. The square-wave behaves like the pancreatic β -cells and the Hindmarsh–Rose model. The elliptic bursting phenomena have been observed in rodent trigeminal interneurons.

4.1. Square wave burster (“fold/homoclinic” burster)

First, we have built the well-known square-wave (or fold/homoclinic) burster [Izhikevitch, 2000; Hoppenstead & Izhikevitch, 1997]. This burster

displays oscillations between a stable limit cycle and a stable node. In Fig. 7(a) we have found a small region of bistability between an oscillatory state with an homoclinic connection and a stable node. If we sketch the behavior of V_m along the line l_4 drawn in Fig. 7(a), a graph similar to the one displayed in Fig. 9(a) is obtained. The bistable regime can be seen on the bifurcation diagram appearing in Fig. 9(a). Although this bistable regime only occurs in a narrow range of I we can apply the technique to this case. Here the transition between the two states takes place through a fold bifurcation for the passage from the resting point to spiking activity and through a homoclinic connection of the saddle point for the transition from firing to resting.

In Fig. 9(b) we have an example of a bursting oscillation between two attractors in the three-dimensional phase space. We also plot the

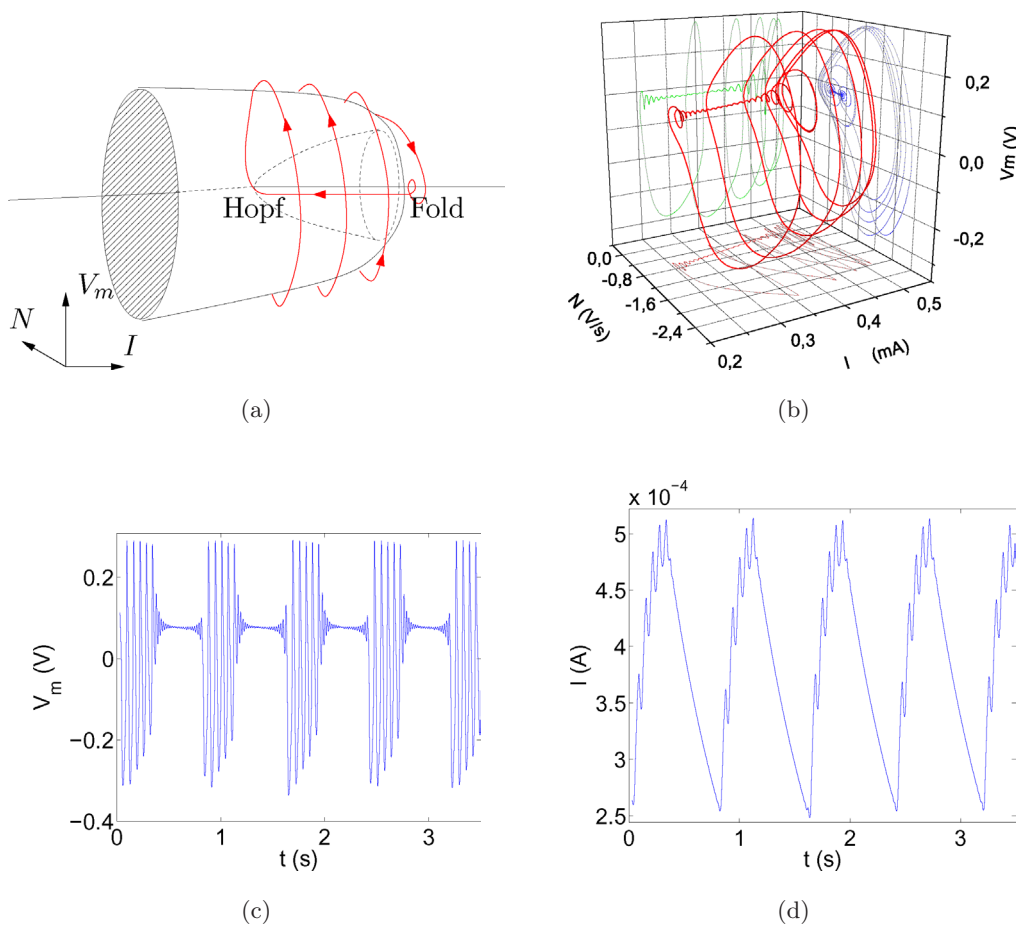


Fig. 10. (a) Bursting behavior of the elliptic burster. The bursting is produced through a subcritical Hopf bifurcation. The gray shade represents the limit cycle and the solid line the stable state. (b) View of the phase space of the system, the variables are (V_m, N, I) , parameters are as follows: $\tau = 0.079$ s, $V_4 = 0.07$ V, $V_3 = 0.12$ V, $V_2 = 0.15$ V, $V_1 = 0$, $g_K^* = 8$ mS, $g_{Ca}^* = 4$ mS, $g_L = 2$ mS, $R_a = 174$, $C_2 = 1 \mu F$, k Ω and $R_b = 10$ k Ω . (c) Time series generated by an elliptic burster built from the Morris–Lecar circuit. Observe the growing of the oscillation as the subcritical Hopf bifurcation is approached. (d) Time series of the current I .

corresponding time series of the voltage in Fig. 9(c), where the temporal characteristics of the bursting are clear.

4.2. *Elliptic burster* (“*subHopf/fold cycle*” *burster*)

We have simulated also the elliptic burster. Once again the bistability is the key point. But in this case the nature of the bifurcation is totally different. In Fig. 10(b) we have a representation of the oscillation in the full three-dimensional phase space. The solid red line corresponds to the trajectory in phase space. The transition from the resting to the spiking regime takes place through a subcritical Hopf bifurcation and the reverse transition occurs through the tangent bifurcation where the unstable limit cycle collapses with the stable cycle. This bifurcation is

also called a “fold cycle”. This kind of behavior can be seen along the line l_2 in Fig. 6(a), where we can see a bistable region due to the subcritical Hopf bifurcation. We can configure this system to oscillate along the line l_2 .

In Fig. 10(b) we represent the experimental phase space, which consists in a three-dimensional space spanned by the membrane voltage, the current and the potassium channel activation. In Fig. 10(c) we have plotted the time series of the voltage V_m . Figure 10(d) depicts the variation of the excitation current.

4.3. “*Circle/fold cycle*” *burster*

This kind of bursters is slightly different from the previous one. There are three different transitions. We have drawn the line l_3 in the bifurcation diagram

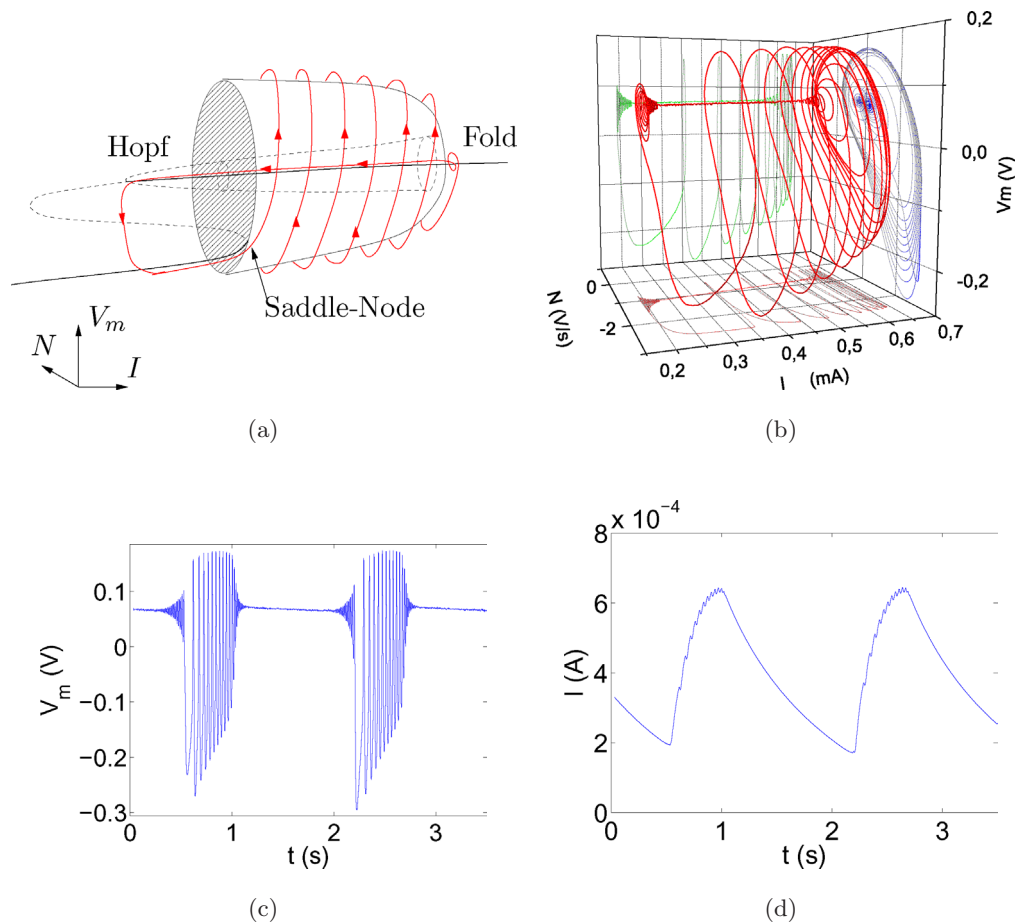


Fig. 11. (a) Dynamical behavior of the circle/fold burster. The transition from the resting to the oscillatory state is made through a saddle-node bifurcation on a limit cycle. The cycle collapses by a fold bifurcation and the system remains in a stable state until it returns to the resting state through a subcritical Hopf bifurcation. (b) Experimental measurement of the attractor as viewed in the three-dimensional phase space (V_m, N, I). The parameter values are as follows: $\tau = 0.026$ s, $V_4 = 0.07$ V, $V_3 = 0.12$ V, $V_2 = 0.15$ V, $V_1 = 0$, $g_K^* = 8$ mS, $g_{Ca}^* = 4$ mS, $g_L = 2$ mS, $C_2 = 1$ μ F, $R_a = 4.3$ k Ω and $R_b = 10$ k Ω . (c) Time series of V_m . (d) Time series of the current I .

in Fig. 6(a). Along this line we have some different bistable states. First, we observe the bistability with two stable nodes and then with a stable node and a stable limit cycle.

The bursting starts after a saddle-node bifurcation on a limit cycle. The electric current keeps increasing until the tangent bifurcation (the fold-cycle bifurcation) takes place and then the system gets back to a new stable node. The current is now decreasing and is reduced until the subcritical Hopf bifurcation occurs. Once this bifurcation is crossed the system returns to the first stable state and the cycle starts over. We summarize this complex behavior in Fig. 11 where we can clearly see how the sequence of attractors is followed by the dynamical system. In panel (a) we have plotted a schematic view of the phase space. In (b) a view of the experimental attractor in the three-dimensional phase space is depicted, panel (c) shows the temporal evolution of the membrane voltage as the system carries out some cycles of bursting.

5. Conclusions

We have designed and built a circuit that approximates the main dynamical regimes of the well-known Morris–Lecar neuron model. By analyzing the behavior of this system in the phase space in terms of some parameters of the model we have been able to obtain different bursting behaviors where each one of them is characterized by the visiting of a particular succession of attractors of the subsystem by the evolving phase point. Thus, our strategy provides a method to investigate the features of relatively simple dynamical systems giving rise to rather complex cycles in the phase space that appear as the phase point transiently visits a given set of stable attractors of the dynamical subsystem.

We have explored the bifurcation diagram of the simplified ML model to point out and extract the dynamical behaviors. We are looking for bistable states and hysteretic phenomena in the system. An appropriate selection of the attractors and a slow drive current form a complex oscillator with the characteristics of a bursting neuron. Such a circuit can be implemented in a VLSI circuit with some modifications, in such a way that a large assembly of coupled bursting neurons can be simulated.

The implementation of the method by means of an electronic circuit introduces a great flexibility in the real time control of the characteristics of

the system. In particular, this method allow us to carry out a continuous control of the behavior of the system by allowing the continuous observation of the system's output as the parameters are changed. The use of electronic circuits is an advantage in this context because they are physical devices that operate in a real environment and thus they are subject to a great deal of uncontrollable noise. This is in fact the environment where real dynamical systems evolve as neurons and so, our method could provide an approach to analyze the robustness of the dynamics of neuronal models under real situations.

Acknowledgments

This work has been partially supported by the Spanish Ministry of Science and Technology under project number BFM2003-03081, the Advanced and Innovational Research program in Life Science from Mext of Japan, and a financial aid from the Universidad Rey Juan Carlos for a research stay in the University of Tokyo, where part of this work was carried out, is also acknowledged. The authors also thank Dr. K. Tsumoto and Dr. Kohno for their valuable comments.

References

- Binczak, S., Azantsev, V., Nekorkin, V. & Bilbault, J.-M. [2003] "Experimental study of bifurcation in modified Fitzhugh–Nagumo cell," *Electron. Lett.* **39**, 961–962.
- Casado, J. M., Ibarz, B. & Sanjuán, M. A. F. [2004] "Winnerless competition in networks of coupled map neurons," *Mod. Phys. Lett. B* **18**, 1347–1366.
- Chay, T. R., Fan, Y. S. & Lee, Y. S. [1995] "Bursting, spiking, chaos, fractals, and universality in biological rhythms," *Int. J. Bifurcation and Chaos* **3**, 595–635.
- Hoppensteadt, F. C. & Izhikevich, E. M. [1997] *Analysis of Neural Excitability and Oscillations* (Springer).
- Horio, Y. & Aihara, K. [2002] "Chaotic neuro-computer," in *Chaos in Circuit and Systems*, eds. Chen, G. & Ueta, T. (World Scientific, Singapore), pp. 237–256.
- Izhikevich, E. M. [2000] "Neural excitability, spiking and bursting," *Int. J. Bifurcation and Chaos* **10**, 1171–1266.
- Kohno, T. & Aihara, K. [2005] "A MOSFET-based model of a class 2 nerve membrane," *IEEE Trans. Neural Networks* **16**, 754–773.
- Kuznetsov, Y. A. [1998] *Elements of Applied Bifurcation Theory* (Springer).
- Le Masson, S., Laflaquiere, A., Bal, T. & Le Masson, G. [1999] "Analog circuits for modeling biological neural networks: Design and applications," *IEEE Trans. Biomed. Engin.* **46**, 638–645.

- Morris, C. & Lecar, H. [1981] “Voltage oscillations in the barnacle giant muscle fiber,” *Biophys. J.* **35**, 193–213.
- Patel, G., Cymbalyuk, G. S., Calabrese, R. L. & DeWeerth, S. P. [2000] “Bifurcation analysis of a silicon neuron,” *Proc. NIPS’1999*, Vol. 12 (MIT Press), pp. 731–738.
- Rinzel, J. & Ermentrout, B. [1989] “Analysis of neural excitability and oscillations,” *Methods in Neuronal Modeling*, eds. Koch, C. & Segev, I. (MIT Press), pp. 135–169.
- Simoni, M. F., Cymbalyuk, G. S., Sorensen, M. E., Calabrese, R. L. & DeWeerth, S. P. [2004] “A multiconductance silicon neuron with biologically matched dynamics,” *IEEE Trans. Biomed. Engin.* **51**, 342–354.
- Szûcs, A., Varona, P., Volkovskii, A. R., Abarbanel, H. D. I., Rabinovich, M. I. & Selverston, A. I. [2000] “Interacting biological and electronic neurons generate realistic oscillatory rhythms,” *Neurorep.* **11**, 563–569.
- Tsumoto, K., Kitajima, H., Yoshinaga, T., Aihara, K. & Kawakami, H. [2006] “Bifurcation in Morris–Lecar neuron model,” *Neurocomputing* **69**, 293–316.
- Tsuji, S., Ueta, T., Kawakami, H. & Aihara, K. [2004] “A design method of bursting using two-parameters bifurcation diagrams in Fitzhugh–Nagumo model,” *Int. J. Bifurcation and Chaos* **14**, 2241–2252.
- Van Schaik, A. [2001] “Building blocks for electronic spiking neural networks,” *Neural Networks*, **14**, 6–7.
- Zeck, G. & Fromherz, P. [2001] “Noninvasive neuroelectronic interfacing with synaptically connected snail neurons immobilized on a semiconductor chip,” *Proc. Natl. Acad. Sci. USA* **98**, 10457–10462.

Appendix

Parameters Used in the Experiment

Table 1. Equivalence between the parameters of the model and the parameters of Eqs. (6) and (7).

Parameter	Values	Units
τ	$R_{21} \times C_1$	s
V_1	$-V_{cc} \times R_1 / (R_1 + R_2)$	V
V_2	$-R_3 / R_4$	V
V_3	$-V_{cc} \times R_{11} / (R_{11} + R_{12})$	V
V_4	$-R_{13} / R_{14}$	V
g_{Ca}^*	$1 / R_{Ca}$	S
g_K^*	$1 / R_K$	S
g_L	$1 / R_L$	S
OPAMP	UA741	—
V_{cc}	10	V
Mutiplier	AD633	—